# A task-based analytical framework for ultrasonic beamformer comparison

Nghia Q. Nguyen[a] and Richard W. Prager
*Department of Engineering, University of Cambridge, Cambridge CB2 1PZ, United Kingdom*

Michael F. Insana
*Department of Bioengineering and Beckman Institute, University of Illinois at Urbana-Champaign, Urbana, Illinois 61801, USA*

(Received 19 May 2016; accepted 11 July 2016; published online 15 August 2016)

A task-based approach is employed to develop an analytical framework for ultrasound beamformer design and evaluation. In this approach, a Bayesian ideal-observer provides an idealized starting point and a way to measure information loss in practical beamformer designs. Different approximations of this ideal strategy are shown to lead to popular beamformers in the literature, including the matched filter, minimum variance (MV), and Wiener filter (WF) beamformers. Analysis of the approximations indicates that the WF beamformer should outperform the MV approach, especially in low echo signal-to-noise conditions. The beamformers are applied to five typical tasks from the BIRADS lexicon. Their performance is evaluated based on ability to discriminate idealized malignant and benign features. The numerical results show the advantages of the WF over the MV technique in general; although performance varies predictably in some contrast-limited tasks because of the model modifications required for the MV algorithm to avoid ill-conditioning.
 [http://dx.doi.org/10.1121/1.4960607]

[HCS] Pages: 1048–1059

## I. INTRODUCTION

The goal of any ultrasonic beamformer is to generate a narrow pulse-echo beam uniformly over the imaging field.[1] The delay-and-sum (DS) beamformer is still widely used for scanning in weakly scattering media because it offers a good balance of performance, robustness and computational cost. It aligns the signal energy received on individual transducer elements by delaying when each time series is applied, according to the geometric distance from the transducer element to a point target. Appropriately delayed and summed waveforms increase the coherence, which improves the echo signal-to-noise ratio (SNR) and the lateral resolution for one-dimensional (1-D) arrays in proportion to the effective aperture size. However, the DS beamformer does not attempt to correct for the distortions and blurring imposed by the ultrasound beam and correlations among the received waveforms, which reduce image quality.

Advances in low-cost high-performance computing make computationally intensive beamformers more practical. Among them, the MV beamformer has been comprehensively investigated and found to improve image quality by several research groups.[2–7] The method selects receive-channel filters that preserve the desired input signal while minimizing interference and noise at the output. It was first derived by Capon for narrowband signals in seismology,[8] and then expanded by Frost to broadband signals for sensor arrays.[9] Recently, a Wiener filter (WF) beamformer has been developed and applied to ultrasound imaging using the minimum mean-square error (MMSE) criterion.[10,11] It comprises a MV beamformer followed by a Wiener post-filter.[12,13] The WF beamformer is shown to enhance the contrast resolution over the MV especially under low echo SNR conditions. There is also a matched filter (MF) beamformer that maximizes the echo SNR of data.[14] It preserves axial resolution and increases the imaging depth penetration.[15] Because each beamformer is optimized with respect to different criteria, there remains a broader question of how to predict and compare their performance in achieving diagnostic objectives.

Performance of an ultrasonic beamformer can be assessed based on the resolution of the resulting image. However, there are usually trade-offs among such images and none individually can characterize all the potential value of a particular algorithm. The solution to this ambiguity is to evaluate each image based on its usefulness in the task for which it has been acquired. This leads us to a *task-based approach* for evaluating imaging systems.[16] Developing such an analytical framework for evaluating ultrasound beamformers is one of the main subjects of this study.

In the task-based approach, the system is evaluated through the performance of an observer, who infers the object as having a disease or non-disease feature based on the generated image. The observer can be an expert human or an algorithm evaluating criteria based on decision theory.[17] Prominent among the latter is the *Bayesian ideal observer*—often referred to simply as the ideal observer (IO)—that combines all available information to make the decision and thus achieves optimal performance. Major limitations of the IO are the computational complexity and the requirement for complete statistical knowledge of the data under consideration, which is unavailable in clinical environments. However, the IO is well suited for controlled simulation studies, to investigate new technologies and processing methodologies where the underlying system is known.

[a]Electronic mail: nqn20@cam.ac.uk

Previously, we developed the IO analysis while searching for improved sonographic lesion-discrimination performance. We proposed several post-array-summation echo-signal filters that were shown in human observer studies to improve detectability for a panel of tasks related to breast lesion diagnosis.[18,19] In that work, we modeled pulse-echo image formation as a linear transformation of object scattering followed by the addition of acquisition noise. We characterized the RF data using multivariate Gaussian processes. The IO test statistic was related to the task of discriminating cancerous features. It was derived from the *log likelihood ratio* between the probability density functions (pdfs) of the two classes: benign and malignant. This test statistic has guided us in designing echo-signal filters that approximate ideal strategies in the sense of maximizing observer performance on the task being undertaken. We also extended the IO analysis for investigating beamforming strategies to individual transducer elements.[20] We divided each beamformer into two steps, *compression* and *processing*. Both are irreversible and any information loss in either one of them cannot be recovered. By analyzing the structure of the *likelihood ratio*, we found that the MF is the optimal operator to preserve task-relevant information in the compression step. Combining this with earlier work on post-processing,[18] we formed a beamforming strategy that minimizes the information loss during the whole transformation from pre-beamformed RF data to the final B-mode image.

In this paper, we use a single decision variable based on the log-likelihood ratio to derive the post-filtering algorithms as well as the optimality of matched filtering in the compression step.[18,19] This unification allows us to derive two popular beamformers, the MV and WF, as approximations of the general Bayesian strategy, and compare them by analyzing the conditions in which each of these approximations hold. Since these approximations may reduce the potential theoretical advantages of the idealized algorithms, we evaluate the beamformers along with other beamforming strategies on a panel of discrimination tasks using Monte Carlo methods. Our numerical treatment considers the ideal case where the system is linear-shift-invariant (LSI), and the spatiotemporal pulse-echo impulse-response function for each transducer element is known, as are the statistical properties of the scattering and acquisition noise. Performance comparisons of the beamformers applied to lesion imaging tasks are conducted by using observer studies in a manner that generates evaluation metrics equivalent to receiver operating characteristic (ROC) analysis.[17]

Section II provides background information that introduces the Bayesian ideal observer applied to simple two-class discrimination tasks. Section III considers each of the beamformers as different approximations to this idealized Bayesian strategy. In Sec. IV we describe a numerical comparison of the beamformers and present the results. Finally, Sec. V draws the conclusions.

## II. BACKGROUND

### A. System modeling

The ultrasound image formation process is depicted in Fig. 1. The system is described as a device that transfers diagnostic information from the object being scanned to the final B-mode image. The process is partitioned into the acquisition and display stages, denoted by $\mathcal{H}$ and $\mathcal{O}$, respectively.[24,25] The acquisition stage, where information from the object is recorded as RF signals, includes pulse transmission and echo reception, up to and including the beamforming operator $\mathcal{B}$. The display stage includes any post-summation data filtering, envelope detection, scan conversion, and gray-scale mapping leading to the final B-mode image.

For each pulse-echo sequence, a subaperture of the linear array is active for both transmit and receive. Time-series waveforms received on the transducer elements are recorded and then mapped back to the spatial domain to form two-dimensional RF echo data. We use the operator $\mathcal{H}_a$ (Fig. 1) to represent the process of using the subaperture to transmit and only one element $a$ to receive. If we assume operator $\mathcal{H}_a$

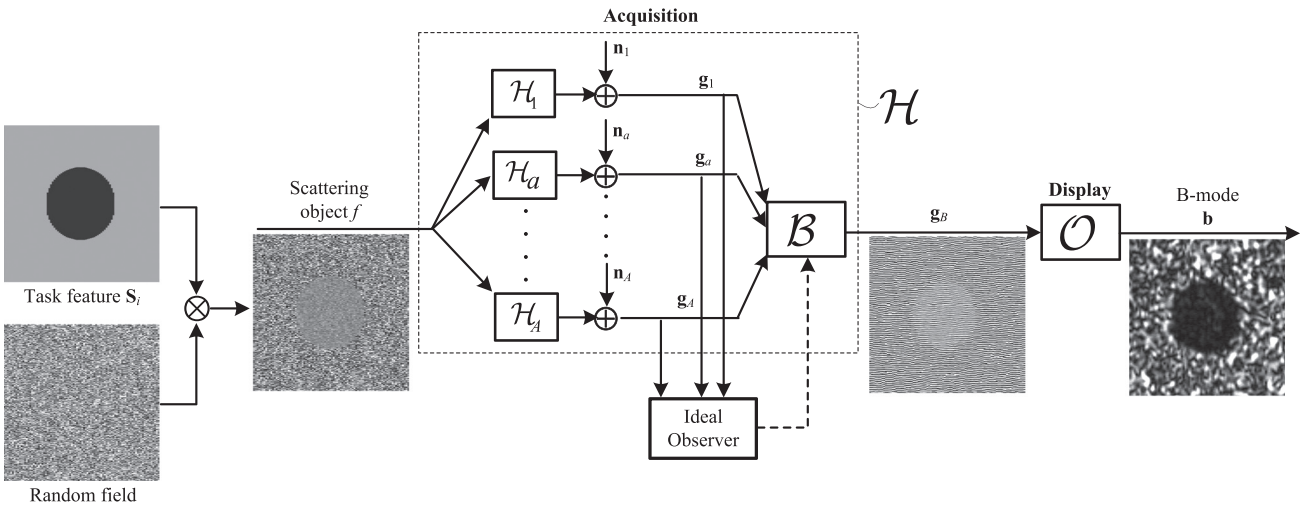


FIG. 1. Diagram of the image formation process, leading to the B-mode image. Each waveform $\mathbf{g}_a$ is recorded from the same scattering object $\mathbf{f}$ but from the perspective of $\mathbf{H}_a$, the pulse-echo system response for the $a$th aperture element. Independent noise $\mathbf{n}_a$ is added to each waveform. The echoes are combined in beamformer $\mathbf{B}$, acting as a linear filter to generate $\mathbf{g}_B = \mathbf{B}^t\mathbf{g}$. Applying operator $\mathcal{O}$ to $\mathbf{g}_B$ and reordering results in a B-mode image. Pre-beamformed echo data is necessary to evaluate new and existing beamforming algorithms in the ideal observer framework.

is linear-shift-invariant (LSI),[26] the entire process can be modeled as a linear convolution in the spatial domain, $h_a(\mathbf{x},t) \underset{\mathbf{x}}{*} f(\mathbf{x})$, where $f(\mathbf{x})$ is 2-D function modeling point scatterers of the weakly scattering medium and $h_a(\mathbf{x},t)$ is the pulse-echo impulse response for receiving element $a$.

By sampling in time with a uniform interval $T$ and lexicographical reordering,[18] we form an $M \times 1$ echo-waveform vector $\mathbf{g}_a(m) = g_a(mT)$ given by the matrix product $\mathbf{H}_a\mathbf{f}$, where $\mathbf{f}$ is an $N \times 1$ column vector re-arranged from the two-dimensional sampled version of $f(\mathbf{x})$, $\mathbf{H}_a$ is a matrix of $M \times N$. The first row of $\mathbf{H}_a$ is a sampled version of the pulse-echo impulse response, $h_a(\mathbf{x},t)$. Other rows are shifted versions of $h_a$, such that convolution $(h_a * f)$ is equivalent to $\mathbf{H}_a\mathbf{f}$. For LSI systems, $\mathbf{H}_a$ is a circulant approximation to a block-Toeplitz matrix that facilitates fast matrix-vector product computations.[18,19] The measurement equation is

$$\mathbf{g}_a = \mathbf{H}_a\mathbf{f} + \mathbf{n}_a, \tag{1}$$

where $\mathbf{n}_a$ is white Gaussian acquisition noise, having size $M \times 1$, zero-mean and covariance $\mathbf{\Sigma}_n$.

The set of pre-beamformed echo waveforms required to form one image frame is expressed as

$$\mathbf{g} = \begin{bmatrix} \mathbf{g}_1 \\ \vdots \\ \mathbf{g}_a \\ \vdots \\ \mathbf{g}_A \end{bmatrix} = \begin{bmatrix} \mathbf{H}_1 \\ \vdots \\ \mathbf{H}_a \\ \vdots \\ \mathbf{H}_A \end{bmatrix} \mathbf{f} + \begin{bmatrix} \mathbf{n}_1 \\ \vdots \\ \mathbf{n}_a \\ \vdots \\ \mathbf{n}_A \end{bmatrix} = \mathbf{H}\mathbf{f} + \mathbf{n}, \tag{2}$$

where $\mathbf{g}$ has size $MA \times 1$ and $\mathbf{H}$ is $MA \times N$. Thus, the pre-beamformed RF data can be considered as the output of a noisy linear transformation of the scattering object.

Beamforming operator $\mathcal{B}$ combines all RF signals from active elements into a single beamformed RF signal, $\mathbf{g}_B$, given by $\mathbf{g}_B = \mathcal{B}\mathbf{g}$. If $\mathcal{B}$ is a linear operator, we can represent it as a matrix $\mathbf{B}$, and $\mathbf{g}_B = \mathbf{B}\mathbf{g}$. The final B-mode image $\mathbf{b}$ is obtained from $\mathbf{g}_B$ through the display stage, $\mathbf{b} = \mathcal{O}\mathbf{g}_B$. For simplicity, we assume some operators, such as low-pass filtering, axial downsampling and lateral interpolation, do not alter the information available in the envelope signal and are ignored. Thus, the display stage includes only the demodulation which is a nonlinear process.

### B. Discrimination tasks

By ignoring coherent scattering, we represent sonograms as spatial patterns of varying incoherent scattering strength.[27] For fully developed speckle, $\mathbf{f}$ is modeled as a zero-mean, stationary, multivariate normal process, where the lesion feature is encoded in the covariance matrix. Specifically, we generate $\mathbf{f}$ by multiplying a 2-D random field by an echogenicity map $\mathbf{S}_i$[28] that carries specific features for a benign $(i=0)$ or malignant $(i=1)$ class. Thus, $\mathbf{f}$ has a Gaussian distribution with the covariance matrix given by $\mathbf{\Sigma}_{obj,i} = \sigma^2_{obj}(\mathbf{I} + \mathbf{S}_i)$, where $\mathbf{S}_i$ is re-arranged into the matrix diagonal to provide the spatial patterns characteristic of the lesion features.[18] In our analysis, we select features from the BIRADS atlas that are sought by radiologists in sonographic examinations when discriminating malignant from benign breast lesions.[29] We use these features to create binary discrimination tasks by defining a malignant $\mathbf{S}_1$ and benign $\mathbf{S}_0$ matrix pair for each task [see Fig. 3(c)]. Observers examine RF or B-mode data sets paired, one from each class, and are asked to classify objects as benign (class 0) or malignant (class 1) based on the data.

In particular, we study five tasks: task 1 involves detecting a low-contrast hypoechoic lesion versus a no-lesion background; task 2 requires discrimination of an elongated eccentric lesion from a circular lesion; task 3 is to discriminate a soft, poorly defined boundary from a well-circumscribed boundary; task 4 requires discrimination of spiculated boundary irregularities from a smooth circular boundary; and task 5 involves discriminating a very weakly scattering hypoechoic interior from an anechoic (cyst-like) lesion interior. Tasks 1 and 5 challenge the system to image large-area diagnostic features (feature area $\gg$ speckle correlation area)[24] while tasks 2–4 relate to lesion boundary features. Task 5 is unique in that it presents the only large-area, high-contrast lesion feature. Tasks with higher complexity features in clinical examination may be synthesized from these five elementary tasks. In each task, the difference between the two features, $\Delta\mathbf{S} = \mathbf{S}_1 - \mathbf{S}_0$, is defined as the *task contrast* that the system delivers to observers of the data. Increasing the task contrast makes the features more obvious to observers. Observers are made fully aware of all visual task features; this is known as the signal-known-exactly condition.

### C. Ideal observer

Our IO analysis begins with standard methods in statistical detection theory.[30] By assuming that $\mathbf{g}$ is a random process with known or measurable distributions, the Neyman-Pearson criteria points to the *log-likelihood ratio* (LLR) as the appropriate discriminator of data between two classes 0 and 1 when the prior probabilities are equal.[30] The LLR classifies the object by comparing the probability of observing $\mathbf{g}$ in each class. We can use the probability density of the data given class $i$, to make comparisons using the LLR test. The LLR rejects the hypothesis that data belongs to hypothesis 0 in favor of hypothesis 1 when scalar test statistic $\lambda$ exceeds threshold $t$. By denoting $p_i(\mathbf{g})$ as the pdf of $\mathbf{g}$ under class $i$, the IO based on the LLR is given by

$$\lambda(\mathbf{g}) = \ln\frac{p_1(\mathbf{g})}{p_0(\mathbf{g})} > t. \tag{3}$$

The observer performance is measured using ROC analysis. At each selected threshold $t$, the true-positive fraction $P_D(t)$ and false-alarm fraction $P_F(t)$ are calculated by $P_D(t) = \Pr\{\lambda(\mathbf{g}) > t | i=1\}$ and $P_F(t) = \Pr\{\lambda(\mathbf{g}) > t | i=0\}$. By sweeping through the possible range of $t$, both $P_D(t)$ and $P_F(t)$ range from 0 to 1. The ROC curve is generated by plotting $P_D(t)$ against $P_F(t)$, and the area under the curve (AUC) is adopted as the observer performance. The LLR test is optimum in the sense that it is guaranteed to yield the

largest true-positive fraction when classifying data into two classes for any fixed value of false-positive fraction. Thus, it achieves the largest AUC and serves as the upper-bound performance for each of the diagnostic tasks.[17]

### D. Calculation of the test statistic

By modeling imaging data $\mathbf{g}$ as a noisy linear transformation of $\mathbf{f}$, we find the pdf of $\mathbf{g}$ under class $i$ is the zero-mean multivariate normal, given by

$$p_i(\mathbf{g}) = \frac{1}{(2\pi)^{MA/2}(\det \boldsymbol{\Sigma}_i)^{1/2}} \exp\left[-\frac{1}{2}\mathbf{g}^t\boldsymbol{\Sigma}_i^{-1}\mathbf{g}\right], \tag{4}$$

where

$$\boldsymbol{\Sigma}_i = \sigma_{obj}^2\mathbf{H}(\mathbf{I}+\mathbf{S}_i)\mathbf{H}^t + \boldsymbol{\Sigma}_n. \tag{5}$$

The covariance matrix now is both nonstationary and nondiagonal because of correlations introduced by the system matrix $\mathbf{H}$. For Gaussian noise, we have $\boldsymbol{\Sigma}_n = \sigma_n^2\mathbf{I}$. From Eq. (4), the test statistic of the ideal observer viewing pre-summed echo data (Fig. 1) is[18]

$$\lambda(\mathbf{g}) = \frac{1}{2}\mathbf{g}^t\left(\boldsymbol{\Sigma}_0^{-1} - \boldsymbol{\Sigma}_1^{-1}\right)\mathbf{g}, \tag{6}$$

where terms independent of $\mathbf{g}$ have been discarded without influencing performance as measured using ROC analysis.[19]

The test statistic of (6) is well defined but the matrix inverses are difficult to calculate because of the large size, $MA \times MA$, of the $\boldsymbol{\Sigma}_i$ matrices. Let us examine the matrix size for a 1-D linear array with a typical pitch of 0.245 mm that scans an imaging region of $30 \times 30\,\text{mm}^2$. Sampling echoes in time at 50 MHz is equivalent to sampling in range with a spatial interval of 0.0154 mm (sound-speed $c = 1540$ m/s). By shifting one element for each scanline, $M = 30/0.0154$ axial pts $\times\, 30/0.245$ scanlines $= 238,500$. With $A = 64$-element active aperture, we have $MA \simeq 1.53 \times 10^7$. Thus $\boldsymbol{\Sigma}_i$ is too large to be inverted straightforwardly.

To compute the test statistic, we apply the *power-series expansion* to each inverse.[31] We first decompose each matrix into stationary and non-stationary components,

$$\Sigma_i = \Sigma_s + \Delta\Sigma_i\,, \text{where } \Sigma_s = \sigma_{obj}^2\mathbf{H}\mathbf{H}^t + \Sigma_n \tag{7}$$

is the stationary component that represents the background area for both classes of data. Stationary matrices can be quickly inverted using Fourier techniques.[17] $\Delta\Sigma_i = \sigma_{obj}^2\mathbf{H}\mathbf{S}_i\mathbf{H}^t$ is the non-stationary component that represents the task features relating to class $i$.

To incorporate the non-stationary term into the inversion, $\boldsymbol{\Sigma}_i^{-1}$ is factorized[18]

$$\Sigma_i^{-1} = \Sigma_s^{-1/2}(\mathbf{I} + \Sigma_s^{-1/2}\Delta\Sigma_i\Sigma_s^{-1/2})^{-1}\Sigma_s^{-1/2}, \tag{8}$$

and the quantity in parentheses is expanded in a power series,

$$(\mathbf{I}+\Sigma_s^{-1/2}\Delta\Sigma_i\Sigma_s^{-1/2})^{-1} = \sum_{k=0}^{\infty}(-\Sigma_s^{-1/2}\Delta\Sigma_i\Sigma_s^{-1/2})^k. \tag{9}$$

This sum converges if the magnitude of each of the eigenvalues of $\Sigma_s^{-1/2}\Delta\Sigma_i\Sigma_s^{-1/2}$ is less than one.[31] We have rearranged $\boldsymbol{\Sigma}_i^{-1}$ so that now only the stationary matrices $\boldsymbol{\Sigma}_s^{-1/2}$ are inverted in the expansion and Fourier techniques can be applied. Depending on task complexity, the sum will converge using from just a few, to more than 100, terms and the test statistic calculation is accomplished.

### E. Performance metrics

In the context of two-alternative forced choice (2AFC) methods, the IO performance or the area under ROC (AUC) can be measured as follows. We calculate $\lambda_i = \lambda(\mathbf{g}|i)$ for each pair of $\mathbf{g}$'s generated under each class $i=0$ and $i=1$. From a large number of pairs of $\mathbf{g}$'s, the AUC is measured by the proportion of correct responses $P_c$, i.e., $P_c = \Pr(\lambda_1 > \lambda_0) = \text{AUC}$.[17] The AUC is then converted to a *detectability index* $d_A$ using

$$d_A = 2\text{erf}^{-1}(2\text{AUC} - 1), \tag{10}$$

where $\text{erf}^{-1}$ is the inverse error function. In a 2AFC study, the AUC ranges from 0.5 to 1 thus $d_A$ ranges from 0 to $\infty$. It is a measure of the task-relevant information available in the echo RF data.[24,25]

## III. BEAMFORMERS AS APPROXIMATIONS TO BAYESIAN STRATEGY

### A. Post-filtering strategies at low contrast

Previously, we showed that if the objective is to increase diagnostic information in the final B-mode image, then Wiener filtering is an optimal strategy to apply to the RF echo signal before demodulation.[18] This result was derived by assuming that the data comprises low-contrast features ($\mathbf{S}_i \simeq \mathbf{0}$) and is already DS beamformed. We now summarize this derivation as it has had a significant influence on our approach to beamformer design.

The IO analysis developed on the DS beamformed data $\mathbf{g}_{DS}$, still includes the same Eqs. (4)–(9) leading to the calculation of the test statistic. However, the sizes of corresponding vectors and matrices are much smaller as they are for compressed data. For convenience, we still use the same notation for the test statistic $\lambda$ and the matrices $\mathbf{H}$, $\Sigma_i$, $\Sigma_s$, and $\mathbf{I}$, but note that they have different dimensions.

First, we truncate the power series expansion in Eq. (9) at the first term to obtain

$$(\mathbf{I} + \Sigma_s^{-1/2}\Delta\Sigma_i\Sigma_s^{-1/2})^{-1} \simeq \mathbf{I} - \Sigma_s^{-1/2}\Delta\Sigma_i\Sigma_s^{-1/2}. \tag{11}$$

Substituting into (8), we have

$$\Sigma_0^{-1} - \Sigma_1^{-1} \simeq \sigma_{obj}^2\Sigma_s^{-1}\mathbf{H}\Delta\mathbf{S}\mathbf{H}^t\Sigma_s^{-1}, \tag{12}$$

where $\Delta\mathbf{S} \triangleq \mathbf{S}_1 - \mathbf{S}_0$ is the task contrast. This approximation holds for the low-contrast discrimination task, or $\text{diag}(\mathbf{S}_{0,1}) \ll 1$. Combining with (6), the first-order approximation of the test statistic is given by

$$\lambda(\mathbf{g}_{DS}) \simeq \frac{1}{2}(\mathbf{W}\mathbf{g}_{DS})^t \Delta\mathbf{S}\mathbf{W}\mathbf{g}_{DS}, \tag{13}$$

where $\mathbf{W} \triangleq \sigma_{obj}\mathbf{H}^t\Sigma_s^{-1}$, which may be recognized as a form of Wiener filtering.

Equation (13) suggests that the WF should be applied to RF data for two reasons. First, it shows that the IO makes an optimal decision based on the task contrast from the Wiener filtered data $\mathbf{W}\mathbf{g}_{DS}$, hence $\mathbf{W}$ only suppresses noise and information that is unrelated to the task. Second, if the imaging system is perfect (i.e., no noise and no blurring), the generated data $\mathbf{g}_{DS}$ is a scaled copy of the scattering object $\mathbf{f}$. In that case, the test statistic is given by $\lambda(\mathbf{f}) = 1/(2\sigma_{obj}^2)\mathbf{f}^t((\mathbf{I} + \mathbf{S}_0)^{-1} - (\mathbf{I} + \mathbf{S}_1)^{-1})\mathbf{f}$. By using the same low-contrast approximation, we have $\lambda(\mathbf{f}) = 1/(2\sigma_{obj}^2)\mathbf{f}^t\Delta\mathbf{S}\mathbf{f}$. There is thus significant equivalence between $\mathbf{W}\mathbf{g}_{DS}$ and $\mathbf{f}$ even when the underlying system becomes realistic. This interpretation is valid when the approximation in (11) is accurate, which only holds for low-contrast tasks. We have shown previously that the WF enhances observer performance including subjective assessment by individuals.[18,19]

In Sec. III B, we start by separating a beamformer into compression and processing steps and show that matched filtering can provide an effective operator to compress presummed echo data. A similar result has been presented in our recent study but based on the *likelihood ratio*.[20] In this paper, we use a test statistic based on the LLR in (6). This helps us to unify the derivations of both compression and processing into the same analysis of a decision variable that leads us to the array-processing techniques found in literature.[12]

### B. MF beamformer

We apply the matrix-inversion lemma in Appendix D to each data covariance matrix given in (5) to obtain

$$\Sigma_i^{-1} = \Sigma_n^{-1} - \sigma_{obj}^2\Sigma_n^{-1}\mathbf{H}((\mathbf{I} + \mathbf{S}_i)^{-1} + \mathbf{K}_n)^{-1}\mathbf{H}^t\Sigma_n^{-1}, \tag{14}$$

where

$$\mathbf{K}_n \triangleq \sigma_{obj}^2\mathbf{H}^t\Sigma_n^{-1}\mathbf{H}. \tag{15}$$

Matrix $\mathbf{K}_n$ plays an important role in our analysis; its trace is the echo SNR and its off-diagonal elements describe point-reflector correlations among the receive-channel echo signals.

Further defining $\mathbf{\Psi}_i \triangleq (\mathbf{I} + \mathbf{S}_i)^{-1} + \mathbf{K}_n$, the test statistic becomes

$$\lambda(\mathbf{g}) = \frac{\sigma_{obj}^2}{2}\mathbf{g}^t\Sigma_n^{-1}\mathbf{H}\left(\Psi_1^{-1} - \Psi_0^{-1}\right)\mathbf{H}^t\Sigma_n^{-1}\mathbf{g}. \tag{16}$$

This step reveals the first routine of the IO. Under white Gaussian noise, $\mathbf{\Sigma}_n = \sigma_n^2\mathbf{I}$, the term $\mathbf{H}^t\mathbf{\Sigma}_n^{-1}\mathbf{g}$ can be recognized as matched filtering on the RF data. Because $\mathbf{g}^t\mathbf{\Sigma}_n^{-1}\mathbf{H} = (\mathbf{H}^t\mathbf{\Sigma}_n^{-1}\mathbf{g})^t$, the IO combines the pre-summed $\mathbf{g}$ vector with the MF, squares and multiplies it by $\mathbf{\Psi}_1^{-1} - \mathbf{\Psi}_0^{-1}$ to form the variable on which the classification decision is based. Since optimal performance can still be achieved after this irreversible step, all of the relevant information must be contained in $\mathbf{H}^t\mathbf{g}$. We name this operator the MF beamformer.

Comparing to Eq. (13), however, the derivation is still incomplete because $\mathbf{\Psi}_1^{-1} - \mathbf{\Psi}_0^{-1}$ is not the task contrast $\Delta\mathbf{S}$. Previously, we showed that there was loss of information in B-mode images after matched filtering if nothing further was done.[20] Thus, we continue to explore the closed-form of $\lambda(\mathbf{g})$ from (16) to find an appropriate subsequent operator to apply to MF beamformed data.

### C. MV beamformer

Assuming $\mathbf{K}_n$ in Eq. (15) is nonsingular (not a good assumption, as we will see), we apply the matrix inversion lemma to $\mathbf{\Psi}_i = \mathbf{K}_n + (\mathbf{I} + \mathbf{S}_i)^{-1}$ to find

$$\mathbf{\Psi}_i^{-1} = \mathbf{K}_n^{-1} - \mathbf{K}_n^{-1}(\mathbf{I} + \mathbf{S}_i + \mathbf{K}_n^{-1})^{-1}\mathbf{K}_n^{-1}. \tag{17}$$

Substituting (17) into (16), we have

$$\lambda(\mathbf{g}) = \frac{\sigma_{obj}^2}{2}\mathbf{g}^t\Sigma_n^{-1}\mathbf{H}\mathbf{K}_n^{-1}\left(\mathbf{\Phi}_0^{-1} - \mathbf{\Phi}_1^{-1}\right)\mathbf{K}_n^{-1}\mathbf{H}^t\Sigma_n^{-1}\mathbf{g}, \tag{18}$$

where $\mathbf{\Phi}_i \triangleq \mathbf{I} + (\mathbf{K}_n^{-1} + \mathbf{S}_i)$. Up to this point, the equation is exact. Applying the power series and retaining just the first term as we did in Eq. (11), we get the approximation

$$\mathbf{\Phi}_i^{-1} \simeq \mathbf{I} - (\mathbf{K}_n^{-1} + \mathbf{S}_i) \text{ and } \mathbf{\Phi}_0^{-1} - \mathbf{\Phi}_1^{-1} \simeq \mathbf{S}_1 - \mathbf{S}_0 = \Delta\mathbf{S}. \tag{19}$$

Consequently, (18) becomes

$$\lambda(\mathbf{g}) \simeq \frac{1}{2}\mathbf{g}_{MV}^t\Delta\mathbf{S}\,\mathbf{g}_{MV}, \tag{20}$$

where $\mathbf{g}_{MV} = \mathbf{B}_{MV}^t\mathbf{g}$ and

$$\begin{aligned}\mathbf{B}_{MV}^t &\triangleq \sigma_{obj}\mathbf{K}_n^{-1}\mathbf{H}^t\mathbf{\Sigma}_n^{-1} \qquad \text{(MV–BF)}\\ &= (\sigma_{obj}\mathbf{H}^t\Sigma_n^{-1}\mathbf{H})^{-1}\mathbf{H}^t\Sigma_n^{-1}.\end{aligned} \tag{21}$$

In Appendix A, we show that Eq. (21) is essentially the same as the Frost beamformer, given by[9]

$$\mathbf{B}_F^t = (\sigma_{obj}\mathbf{H}^t\Sigma_g^{-1}\mathbf{H})^{-1}\mathbf{H}^t\Sigma_g^{-1}, \tag{22}$$

where $\mathbf{\Sigma}_g$ is either $\mathbf{\Sigma}_0$ or $\mathbf{\Sigma}_1$, the power of the output data. The Frost beamformer in Eq. (22) decorrelates the data by minimizing its power while preserving the main signals. Thus, it is equivalent to the whitening process in Eq. (21) that minimizes noise only.

The Frost beamformer was designed for *broadband* data. It jointly decorrelates the data among transducer elements in both the spatial and temporal domains. In our analysis, the source of spatial and temporal correlations can be seen by examining the system matrix $\mathbf{H}$, constructed from the pulse-echo spatiotemporal impulse response.[26]

We show that the MV beamformer $\mathbf{B}_{MV}^t$ follows the ideal observer strategy exactly to the point where the approximation of Eq. (19) is made. Equation (20) performs well when $\mathbf{K}_n^{-1}$ is small, and the deviation of the task-area variance from the surrounding region, $\mathbf{S}_i$, is small. In Sec. III D, we form a better first-order approximation to the inverse of $\mathbf{\Phi}_i$.

### D. WF beamformer

In Eq. (18), we express $\mathbf{\Phi}_i = \mathbf{\Phi}_s + \mathbf{S}_i$, where $\mathbf{\Phi}_s = \mathbf{I} + \mathbf{K}_n^{-1}$ is the task-independent *stationary* covariance term for the region in the object surrounding task area $\mathbf{S}_i$. This reassociation of terms leads to a different approximation than that made in the MV beamformer derivation. Using Eqs. (8) and (9) and retaining just the first-order term in the expansion, the covariance inverse is

$$\begin{aligned}\mathbf{\Phi}_i^{-1} &= \mathbf{\Phi}_s^{-1/2}(\mathbf{I} + \mathbf{\Phi}_s^{-1/2}\mathbf{S}_i\mathbf{\Phi}_s^{-1/2})^{-1}\mathbf{\Phi}_s^{-1/2} \\ &\simeq \mathbf{\Phi}_s^{-1} - \mathbf{\Phi}_s^{-1}\mathbf{S}_i\mathbf{\Phi}_s^{-1}, \end{aligned} \tag{23}$$

so that

$$\mathbf{\Phi}_0^{-1} - \mathbf{\Phi}_1^{-1} \simeq \mathbf{\Phi}_s^{-1}\Delta\mathbf{S}\mathbf{\Phi}_s^{-1} = (\mathbf{I}+\mathbf{K}_n^{-1})^{-1}\Delta\mathbf{S}(\mathbf{I}+\mathbf{K}_n^{-1})^{-1}, \tag{24}$$

and the task matrix is diagonalized. Substituting (24) into (18), the test statistic becomes

$$\begin{aligned}\lambda(\mathbf{g}) &\simeq \frac{\sigma_{obj}^2}{2}\mathbf{g}^t\mathbf{\Sigma}_n^{-1}\mathbf{H}\mathbf{K}_n^{-1}\left(\mathbf{I}+\mathbf{K}_n^{-1}\right)^{-1}\Delta\mathbf{S} \\ &\quad\times \left(\mathbf{I}+\mathbf{K}_n^{-1}\right)^{-1}\mathbf{K}_n^{-1}\mathbf{H}^t\mathbf{\Sigma}_n^{-1}\mathbf{g} \\ &= \frac{\sigma_{obj}^2}{2}\mathbf{g}^t\mathbf{H}\mathbf{\Omega}_s^{-1}\Delta\mathbf{S}\mathbf{\Omega}_s^{-1}\mathbf{H}^t\mathbf{g} \\ &= \frac{1}{2}\mathbf{g}_{WF}^t\Delta\mathbf{S}\,\mathbf{g}_{WF}, \end{aligned} \tag{25}$$

where

$$\mathbf{\Omega}_s^{-1}\mathbf{H}^t = (\mathbf{I}+\mathbf{K}_n^{-1})^{-1}\mathbf{K}_n^{-1}\mathbf{H}^t\mathbf{\Sigma}_n^{-1} = (\sigma_{obj}^2\mathbf{H}^t\mathbf{H}+\sigma_n^2\mathbf{I})^{-1}\mathbf{H}^t.$$

The last form assumes $\mathbf{\Sigma}_n = \sigma_n^2\mathbf{I}$. Also $\mathbf{g}_{WF} = \mathbf{B}_{WF}^t\mathbf{g}$ for

$$\begin{aligned}\mathbf{B}_{WF}^t &\triangleq \sigma_{obj}\mathbf{\Omega}_s^{-1}\mathbf{H}^t \quad \text{(WF–BF)} \\ &= \sigma_{obj}(\sigma_{obj}^2\mathbf{H}^t\mathbf{H} + \sigma_n^2\mathbf{I})^{-1}\mathbf{H}^t, \end{aligned} \tag{26}$$

which is the WF beamformer for Gaussian acquisition noise. Here matched and regularized inverse filters are applied to each receive channel before summation to restore coherence and spatial resolution.

### E. Comparing MV and WF

The differences between $\mathbf{B}_{MV}^t$ and $\mathbf{B}_{WF}^t$ are the corresponding approximations made in (19) and (23), respectively. To explore this aspect more deeply, we need the Fourier transform of positive-definite $\mathbf{K}_n$. That is, $\tilde{\mathbf{K}}_n = \mathbf{F}\mathbf{K}_n\mathbf{F}^{-1}$ where $\mathbf{F}$ is the 2-D discrete Fourier-transform (DFT) matrix. Spectral values at each spatial frequency are eigenvalues of $\mathbf{K}_n$ under the conditions we are considering. Their magnitude must remain less than one for the approximations to remain valid. Violations of this condition lead to poor beamforming performance.

First, consider the MV approximation of (19). $\mathbf{K}_n$ describes the echo-signal energy within and between receive channels divided by the acquisition-noise energy. Therefore $\tilde{\mathbf{K}}_n$ is akin to an echo-SNR frequency spectrum. When the echo SNR is high, the approximation works well provided feature contrast via $\max(\mathbf{S}_i)$ is low. However, at frequency channels where the noise energy exceeds the signal energy, the magnitude of the eigenvalues of $(\mathbf{K}_n^{-1} + \mathbf{S}_i)$ in (19) exceed one. When this occurs, low-rank approximation methods can reduce the rank of the matrix appropriately, as we show in Appendix B. Without these approximations, the MV beamformer can be unstable.

Next consider the WF approximation of (23). The eigenvalues of $(\mathbf{I}+\mathbf{K}_n^{-1})^{-1/2}\Delta\mathbf{S}(\mathbf{I}+\mathbf{K}_n^{-1})^{-1/2}$ must be small for this approximation to hold. Hence the frequency spectrum of $(\mathbf{I}+\mathbf{K}_n^{-1})^{-1/2}$ is the controlling factor. At high echo SNR, the factor is approximately one, so as long as $|\Delta\mathbf{S}|$ is small or low contrast features, the approximation is valid. At low echo SNR, $(\mathbf{I}+\mathbf{K}_n^{-1})^{-1/2}$ is always small. Although both beamformers require low contrast features, MV also requires high echo SNR while WF can tolerate low echo SNR conditions. The superior performance of WF over MV in a low echo SNR condition was observed by Nilsen and Holm in their study.[10]

## IV. NUMERICAL STUDY

### A. Simulation

We performed a numerical study where the pulse-echo spatiotemporal impulse response at each transducer element is generated using the Field II program.[21,22] The simulation is based on the parameters of the ULA-OP ultrasound system[23] (developed at MSD Laboratory, Università degli Studi di Firenze, Florence, Italy). A linear array probe (LA523, Esaote spa, Florence, Italy) was used. This linear array has 192 elements each of dimensions $0.215 \times 6.0\,\text{mm}^2$ separated by a 0.03 mm kerf. There are 64 elements active in each transmit and receive cycle. A 20-mm transmit/receive focal length was used. In elevation, the aperture is weakly focused using an acoustic lens with a focal length of 20 mm. A three-cycle excitation voltage is applied to generate an ultrasound pulse with center frequency at 6.0 MHz and a 40% pulse-echo bandwidth. The RF echo signals were sampled at 50 Msamples/s, resulting in an axial sampling interval of 0.0154 mm. In the lateral direction the beam is stepped by an element pitch of 0.245 mm. However, we remove the need for interpolation in the display stage by generating impulse responses with lateral spacing 0.049 mm. The impulse responses are used to construct matrix $\mathbf{H}_a$ at each received channel $a$ and the overall system matrix $\mathbf{H}$. The noise variance $\sigma_n^2$ was adjusted so that the echo SNR for the DS beamformed RF signals is 24 dB.

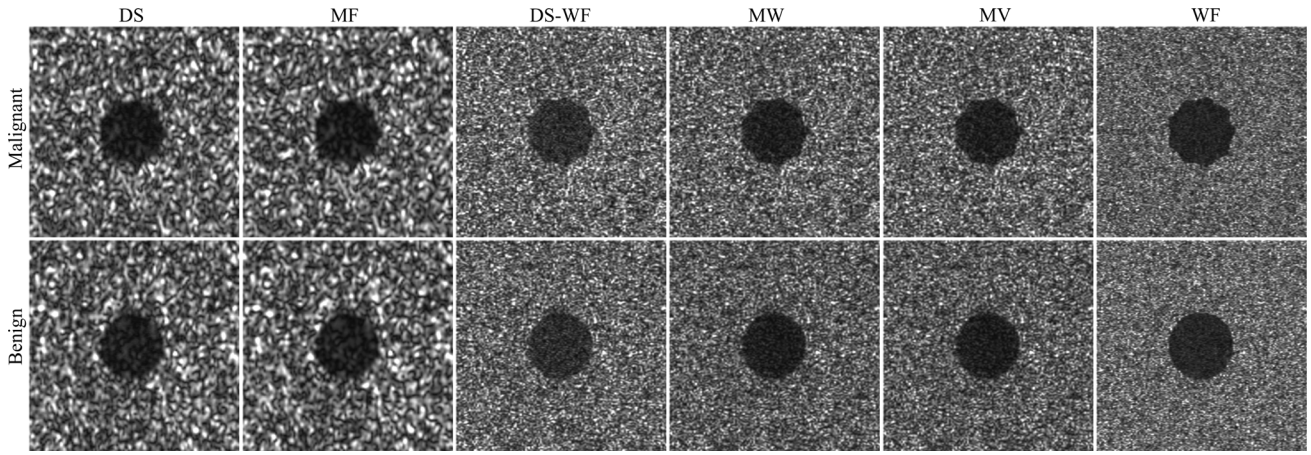


FIG. 2. Examples of image pairs (linear scale) for task 4 [spiculate (top row) vs circular (bottom row)] using the same receive-channel echo data after applying beamformers in various combinations. MF is without post-summation filtering (step 1 only); DS-WF is Wiener filtering after DS beamforming; MW is Wiener filtering after MF beamforming.

### B. Beamforming implementation

Beamformers were applied to each data set before displaying the result as B-mode images. Under the circulant assumption for each $\mathbf{H}_a$, the MF, MV, and WF beamformers are easily implemented using a 2-D DFT technique.[18] Because $\mathbf{H}^t\mathbf{H}$ can be ill-conditioned, the MV beamformer requires an approximation to improve its robustness. In this work, we use a reduced-rank approximation to for the implementation. This is equivalent to projecting the data into a stable subspace before performing the decorrelation function of the MV beamformer.[32] The eigenvalues of the matrix $\mathbf{H}^t\mathbf{H}$ are calculated and normalized to the largest eigenvalue. We retain eigenvalues above the level of −38 dB. This threshold is selected by visually balancing the MV performance among the five feature tasks. In our simulations, the percentage of pulse energy contained in the discarded sub-threshold eigenvalues is less than 0.05% of the total and is assumed to be negligible. However, the reduced-rank approximation also slightly changes the system matrix, $\mathbf{H}$, which can influence the predictions from the analysis.

We also implement the strategies developed in previous studies,[18,20] and compare them to the MV and WF beamformers. Specifically, we apply the WF to the DS beamformed and MF beamformed data. We name the first combination the DS-WF beamformer. The second combination, using the WF and MF is analyzed in Appendix C. It is equivalent to the WF beamformer but requires some modification to avoid $\mathbf{H}^t\mathbf{H}$ being ill conditioned. By using the same reduced-rank approximation adopted in the MV implementation, this beamformer can serve as a transitional step between the MV and full-size WF beamformers. We name it the matched Wiener (MW) beamformer.

Examples of B-mode image pairs for task 4 are shown in Fig. 2. Different combinations of beamforming strategies were applied to the same set of simulated receiver-channel echo data. The variance profiles of task 4 are shown in the fourth column of Fig. 3(c). The task is designed for discriminating between the regular (circular) and the irregular shape (spiculate) lesions. The results show that the advanced beamformers make the features easier to discriminate than in the image pair generated by the DS beamformer. But the image pair generated by the MF beamformer, where there is compression without any filtering, offer no gain in discrimination. The improvements are quantified using observer efficiencies as presented in Sec. IV C.

### C. Observer efficiency

Since each task is designed for a specific feature, we place them on a common scale using an object contrast factor, defined by

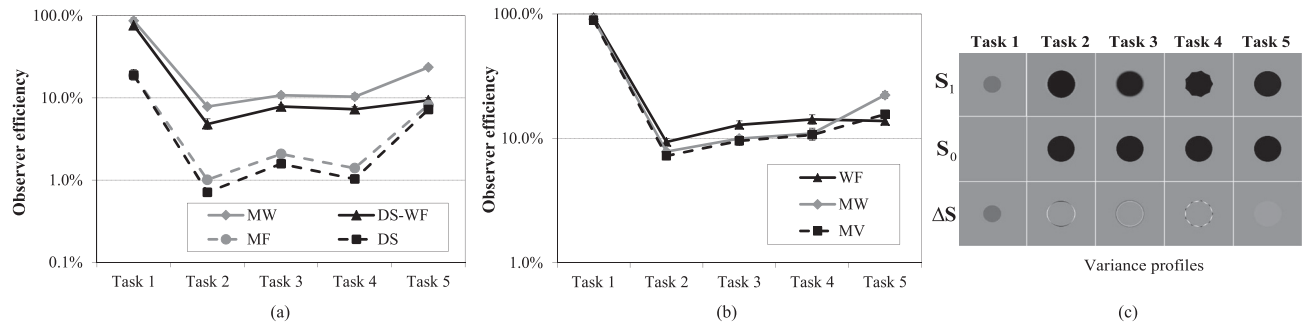


FIG. 3. Observer efficiencies measured for the beamformers illustrated in Figs. 2 are plotted (log-scale) in (a) and (b) with five discrimination tasks. Note that the log-scales in the two plots are different from each other. (c) Variance profiles are shown for five tasks.

$$C = \sum_j |[\Delta \mathbf{S}]_{jj}|. \tag{27}$$

We assume that the sample intervals in the lateral and axial directions of the variance profiles are the same for every task. In Eq. (27), $[\Delta \mathbf{S}]_{jj}$ is element $j$ on the main diagonal. The factor $C$ takes values in the range from 0 to $\infty$. Increasing $C$ makes the features more obvious to observers.

The observer efficiency is used to measure the loss of information as it is transferred from the pre-beamformed RF data to the final B-mode image. It can be used to quantify the performance of each beamformer on the five lesion-feature tasks.[20] The task-relevant information in the beamformer output is measured through the observer performance. First, we compute the proportion of correct responses, $P_c$, for the IO via Eq. (4) operating on pre-summed echo data. It is calculated in a 2AFC Monte Carlo study involving 2000 image pairs for each evaluation reported. Similar to our earlier studies,[18–20] we measure the information available in the B-mode images using the Smith-Wagner (SW) observer.[33,34] The test statistic is given by[18]

$$\lambda_{SW}(\mathbf{b}) = \mathbf{b}^t \Delta \mathbf{S}\, \mathbf{b}, \tag{28}$$

where $\mathbf{b}$ is the column vector of a B-mode image acquired with a particular beamformer. The SW observer is an approximation of the IO on B-mode images for task 1 and its performance is highly correlated to that of human observers.[33,34] In this study, we use it to approximate the IO on B-mode images for all five tasks. We measure the SW observer performance also in terms of the proportion correct $P_c$ by applying the observer to B-mode image obtained with different beamformers. The standard observer efficiency is then given by

$$\eta = (d_{A,I}/d_{A,SW})^2, \tag{29}$$

where $d_{A,I}$ and $d_{A,SW}$ are the detectability indices converted from the performance of the ideal and SW observer calculated with the same object contrast factor. As $P_c \mapsto 1$, however, the $d_A$ approaches infinity making the calculation unstable. Thus, we modify the calculation using the object contrast factors.[18] We proceeded by adjusting the contrast $C_{SW}$ for each task until the SW observer achieved $P_c \simeq 0.8$. We then reduced the contrast until the ideal observer also achieve the same $P_c$ to find $C_I$. The observer efficiency is given by

$$\eta = (C_I/C_{SW})^2. \tag{30}$$

The efficiency has error bars calculated by assuming the correct proportion follows a binomial distribution with mean $p = P_c$. The standard deviation of $P_c$ is given by $\sqrt{(p(1-p)/n)}$ where $n$ is the number of sample ($n = 2000$). This error then is propagated through the task contrast to the efficiency calculation in (30).[18,19]

### D. Results and discussion

Figures 3(a) and 3(b) display the efficiencies of the beamformers for discriminating malignant from benign features in tasks 1–5 where the variance profiles are shown in Fig. 3(c). In all tasks, the DS has the lowest efficiencies, between 0.71% and 19.05%. The MF gives small improvements on each task. Applying the WF to both DS and MF beamformed data, the observer efficiencies of DS-WF and MW have substantial improvements for all tasks especially for task 1 which is the low-contrast detection. Between them, the efficiencies of the MW is higher. The results indicate a better match when using the MF for compressing pre-beamformed echo data.

Although the MF combines all task-relevant information available in pre-summed RF data, it delivers only small improvements in the efficiency. This can be explained by examining the corresponding covariance matrices $\mathbf{\Psi}_i$ in (16). They are non-diagonal suggesting that both magnitude and phase components are retained. As the phase term is removed during demodulation, there is loss of information in the B-mode image. This loss can be partially recovered by applying the corresponding WF before envelope detection.

The efficiencies of MV and WF beamformers are plotted and compared in Fig. 3(b). The figure also includes the MW plot as an intermediate case between the MV and WF. Compared to the MF beamformer, derived from the IO analysis without a filtering step, both WF and MV are substantially more efficient for all the tasks. In task 1, the WF efficiency reaches 94%. Between the WF and MV beamformers, the WF is better in tasks 1–4, but has lower performance in task 5 (13.79% vs 15.61%). We note that the MV is implemented with a reduced-rank approximation that slightly changes the system model. Thus, we compare it to the MW which is the WF implemented with the same modifications. Over the five tasks, the MW has efficiencies that are equivalent or higher as predicted. Between the MW and the WF, the WF has higher efficiencies in tasks 1–4, but lower in task 5. This is because the reduced-rank approximation decreases the ability of the system to transfer high spatial-frequency information into the image. While this loss decreases the WF beamformer effectiveness in tasks 1–4, it provides an advantage for task 5 where the high-frequency channels are occupied mostly by noise. Thus, the observed improvement of the MV over the WF in task 5 comes from the reduced-rank approximation. We note that the MW is the optimal beamforming strategy suggested in our previous study.[20] This shows one of the advantages of the analysis where we unify the derivations of compression and filtering into the same framework using the log-likelihood ratio, which leads us to the derivation of the full-size WF beamformer.

We show in our analysis that the WF offers improvements under low echo SNR conditions. To verify the advantage of the WF, we investigate the efficiencies of WF and MV over variations in the echo SNR. Figures 4(a) and 4(c) plot the MV, MW, and WF efficiencies with echo SNR of 32 dB and 16 dB for tasks 2–5. We also extract those for echo SNR of 24 dB from Fig. 3(b) and plot them in Fig. 4(b). The results are on a linear scale and ranged from 0% to 30%. The efficiencies measured for task 1 are

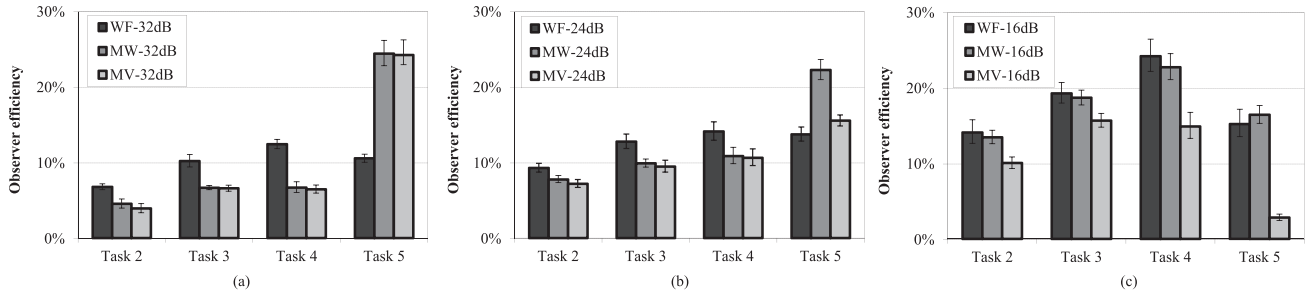


FIG. 4. Efficiency comparisons for WF and MV beamformers with variations of echo SNRs. The results, excluding task 1, are plotted using a linear scale.

out of this range (from 80% to 100%), and are excluded from the figures.

At high echo SNR of 32 dB, the MV and MW efficiencies are almost the same as each other. They are both lower than the WF efficiency in tasks 2–4, but higher in task 5 because of the system modification. This means that the regularization through echo SNR applied to the MW does not have much impact on the beamformer performance. At low echo SNR of 16 dB, however, the MV performance is lowest on all four tasks, especially on task 5 (2.94%). This indicates the instability of the MV at this noise level. Meanwhile, the MW and WF efficiencies are on par to each other. In this echo SNR condition, the reduced-rank approximation does not much affect the beamformer performance. More regularization is needed to avoid ill-conditioning for the MV.

In Fig. 4, we note the beamformer efficiencies are higher at lower echo SNRs. This shows that efficiency is not the same as, or even proportional to, the beamformer performance. Efficiency is calculated using the object contrast factor $C_I$, which at ideal performance reaches 80%. At lower echo SNR, a higher $C_I$ is needed. Although the $C_{SW}$ is also higher, the efficiency, as calculated through the ratio between the two object contrast factors, is increased even when the beamformer performance is reduced.

## V. SUMMARY AND CONCLUSION

The main contribution of this paper is to provide a new statistical framework for evaluating and comparing ultrasound beamformers. We have explored a general Bayesian strategy for beamforming and shown how a number of popular algorithms are adapted to the task in different ways. We have shown how approximate forms of covariance-matrix inverses lead to filters that are equivalent to each of these popular beamforming algorithms; and that they are optimal with respect to MV or MMSE criteria but not necessarily for all object features. In these derivations, we separated the measurement properties of the system from the task to derive a filter that is applied to the pre-summed echo-signal vector $\mathbf{g}$. Each of the filter expressions that we found provide a prescription for the weights (magnitude and phase) to be applied to individual receive-channel data before summation and any post-summation filtering.

In our analysis, we have expressed the MF beamformer in terms of a compressing step plus additional filters that form a processing step. This leads to the derivation of a log likelihood measure of performance and reveals the link to the MV and WF beamformers. In the presence of acquisition noise, the filtering derivations require some approximations and, as a result, the output quality was found to vary with echo SNR, spatial resolution, and task contrast. In our framework, the WF is derived as a better approximation to the ideal strategy than that being used for deriving the MV beamformer. Further analysis has shown the MV beamformer is based on an unregularized solution of the inverse problem. It is unstable with noisy data and requires approximations to improve the robustness. Those based on the WF are the least sensitive to low echo SNR instabilities because of their natural regularization.

We have employed the SW model observer specifically to focus on evaluation of image formation processes in the transfer of task information. This is the objective of beamforming, although a comprehensive clinical-efficacy study would include human observers studies and clinical cases. Note that the SW observer was developed as an approximation of the ideal observer for low-contrast detection. Its performance was also highly correlated to human observer performance on that task.[34] However, these properties are unlikely to perform optimally for the other high-contrast discriminations. This limitation motivates further investigation in the future.

The WF beamformer is derived under the assumption of low-contrast features for the breast lesion. Among the five tasks related to breast cancer diagnosis, it offers the least improvement over the DS beamformer in high-contrast feature discrimination (hypoechoic/anechoic). In the future, we therefore wish to develop a new approximation to relax this constraint.

The MV beamformer derived in our framework is for broadband signals, which jointly decorrelates data in both the spatial and temporal domains. We have shown how its potential benefits in transferring high-frequency information to the final images can be completely negated by model modifications required during implementation. Investigating an implementation that maintains the advantages of MV beamforming will therefore also be a topic for future research.

## ACKNOWLEDGMENT

The authors thank Dr. Craig Abbey of University of California, Santa Barbara for advising and discussing many aspects of this work.

## APPENDIX A: THE FROST ALGORITHM

Frost described a linearly constrained least mean-squares algorithm under conditions where the signal and noise statistics are unknown and estimated from the data (an adaptive algorithm).[9] We applied his time-domain approach using our pulse-echo constraints, and assuming known statistics, to show how it relates to the ideal-observer formalism described in Sec. III C. The goal of the Frost beamformer is to minimize output power while decorrelating and condensing the echo signals. Given the beamformed echo signal is $\mathbf{B}^t\mathbf{g} = \mathbf{B}^t\mathbf{H}\mathbf{f} + \mathbf{B}^t\mathbf{n}$, the output power is minimized by finding $\mathbf{B}^t$ that minimizes $\mathcal{E}\{\frac{1}{2}\mathbf{g}^t\mathbf{B}\mathbf{B}^t\mathbf{g}\} = \frac{1}{2}\mathrm{tr}(\mathbf{B}^t\boldsymbol{\Sigma}_g\mathbf{B})$, while being subject to the constraint $\sigma_{obj}\mathbf{B}^t\mathbf{H} \simeq \mathbf{I}$. Matrix $\boldsymbol{\Sigma}_g$ can be either $\boldsymbol{\Sigma}_1$ or $\boldsymbol{\Sigma}_0$ in our IO analysis depending on the class where the imaging data is considered.

Applying the method of Lagrange multipliers, we form a cost function $C$ involving undetermined Lagrange matrix $\boldsymbol{\Lambda}$,

$$C(\mathbf{B}) = \mathrm{tr}\left[\frac{1}{2}\mathbf{B}^t\boldsymbol{\Sigma}_g\mathbf{B} + \boldsymbol{\Lambda}^t\left(\sigma_{obj}\mathbf{H}^t\mathbf{B} - \mathbf{I}\right)\right]. \tag{A1}$$

Taking the gradient of (A1) with respect to $\mathbf{B}$ and setting the result to zero,

$$\frac{\partial C(\mathbf{B})}{\partial \mathbf{B}} = \boldsymbol{\Sigma}_g\mathbf{B} + \sigma_{obj}\mathbf{H}\boldsymbol{\Lambda} = 0, \tag{A2}$$

we obtain $\mathbf{B} = -\sigma_{obj}\boldsymbol{\Sigma}_g^{-1}\mathbf{H}\boldsymbol{\Lambda}$. Hence,

$$\sigma_{obj}\mathbf{H}^t\mathbf{B} = \mathbf{I} = -\sigma_{obj}^2\mathbf{H}^t\boldsymbol{\Sigma}_g^{-1}\mathbf{H}\boldsymbol{\Lambda}, \tag{A3}$$

and

$$\boldsymbol{\Lambda} = -(\sigma_{obj}^2\mathbf{H}^t\boldsymbol{\Sigma}_g^{-1}\mathbf{H})^{-1} = \boldsymbol{\Lambda}^t. \tag{A4}$$

Thus,

$$\mathbf{B}_F = \mathbf{B} = \boldsymbol{\Sigma}_g^{-1}\mathbf{H}(\sigma_{obj}\mathbf{H}^t\boldsymbol{\Sigma}_g^{-1}\mathbf{H})^{-1}. \tag{A5}$$

Equation (A5) is the well-known form of the Frost beamformer found in the literature.[9,12] As $\boldsymbol{\Sigma}_g$ is equal to $\boldsymbol{\Sigma}_i$ ($i$ is either 0 or 1), we have

$$\boldsymbol{\Sigma}_g^{-1} = [\sigma_{obj}^2\mathbf{H}(\mathbf{I} + \mathbf{S}_i)\mathbf{H}^t + \boldsymbol{\Sigma}_n]^{-1}, \tag{A6}$$

Applying the matrix-inversion lemma (Appendix D) to the right-hand side and simplifying the expression, we are able to obtain

$$\boldsymbol{\Sigma}_g^{-1}\mathbf{H} = \boldsymbol{\Sigma}_n^{-1}\mathbf{H}\Theta^{-1}, \tag{A7}$$

$$\mathbf{H}^t\boldsymbol{\Sigma}_g^{-1}\mathbf{H} = \mathbf{H}^t\boldsymbol{\Sigma}_n^{-1}\mathbf{H}\Theta^{-1}, \tag{A8}$$

where

$$\Theta = (\mathbf{I} + \mathbf{S}_i)[(\mathbf{I} + \mathbf{S}_i)^{-1} + \sigma_{obj}^2\mathbf{H}^t\boldsymbol{\Sigma}_n^{-1}\mathbf{H}]. \tag{A9}$$

Combining (A7), (A8), and (A9) with (A5), we find

$$\mathbf{B}_F = \boldsymbol{\Sigma}_n^{-1}\mathbf{H}(\sigma_{obj}\mathbf{H}^t\boldsymbol{\Sigma}_n^{-1}\mathbf{H})^{-1}. \tag{A10}$$

The $\mathbf{B}_F$ in Eq. (A10) is identical to $\mathbf{B}_{MV}^t$ in Eq. (21). Thus, we have shown that the Frost beamformer derived in the linearly constrained MV approach is equivalent to the MV beamformer derived in our IO analysis.

## APPENDIX B: IMPROVING ROBUSTNESS

If matrix $\mathbf{K}_n$ is poorly conditioned, it may not be possible to apply the matrix-inversion lemma as in Eq. (17). In this Appendix, we modify our derivations in Secs. III C and III D to improve the robustness of the analysis under these conditions. For this purpose, $\mathbf{K}_n$ is modified using a diagonal-loading/regularization approach[12] to ensure the matrix remains positive-definite, $\mathbf{K}_{n,\varepsilon} \triangleq \sigma_{obj}^2\mathbf{H}^t\boldsymbol{\Sigma}_n^{-1}\mathbf{H} + \varepsilon\mathbf{I}$, where $\varepsilon \to 0^+$. It is sufficient to add a small Gaussian random perturbation to the pulse-echo point-spread-function so that $\mathbf{K}_n$ becomes invertible.

Following the treatment leading to (16), the test statistic is now

$$\lambda(\mathbf{g}, \varepsilon) = \frac{\sigma_{obj}^2}{2}\mathbf{g}^t\boldsymbol{\Sigma}_n^{-1}\mathbf{H}\left(\boldsymbol{\Psi}_{1,\varepsilon}^{-1} - \boldsymbol{\Psi}_{0,\varepsilon}^{-1}\right)\mathbf{H}^t\boldsymbol{\Sigma}_n^{-1}\mathbf{g}, \tag{B1}$$

where $\boldsymbol{\Psi}_{i,\varepsilon} = (\mathbf{I} + \mathbf{S}_i)^{-1} + \mathbf{K}_{n,\varepsilon}$ for $i = 0,1$, and $\lambda(\mathbf{g}, \varepsilon) \to \lambda(\mathbf{g})$ as $\varepsilon \to 0^+$. Since $\mathbf{K}_{n,\varepsilon}$ is now invertible, applying the matrix inversion lemma to $\boldsymbol{\Psi}_{i,\varepsilon}^{-1}$ yields

$$\boldsymbol{\Psi}_{i,\varepsilon}^{-1} = \mathbf{K}_{n,\varepsilon}^{-1} - \mathbf{K}_{n,\varepsilon}^{-1}(\mathbf{K}_{n,\varepsilon}^{-1} + \mathbf{I} + \mathbf{S}_i)^{-1}\mathbf{K}_{n,\varepsilon}^{-1}. \tag{B2}$$

Substituting (B2) into (B1), we have

$$\lambda(\mathbf{g}, \varepsilon) = \frac{\sigma_{obj}^2}{2}\mathbf{g}^t\boldsymbol{\Sigma}_n^{-1}\mathbf{H}\mathbf{K}_{n,\varepsilon}^{-1}\left(\boldsymbol{\Phi}_{0,\varepsilon}^{-1} - \boldsymbol{\Phi}_{1,\varepsilon}^{-1}\right)\mathbf{K}_{n,\varepsilon}^{-1}\mathbf{H}^t\boldsymbol{\Sigma}_n^{-1}\mathbf{g}, \quad \text{where } \boldsymbol{\Phi}_{i,\varepsilon} = \mathbf{I} + \mathbf{K}_{n,\varepsilon}^{-1} + \mathbf{S}_i. \tag{B3}$$

Method 1: Applying the series expansion of (9) to (B3), where $\mathbf{I}$ is separated from $\mathbf{K}_{n,\varepsilon}^{-1} + \mathbf{S}_i$, we obtain the approximations

$$\boldsymbol{\Phi}_{i,\varepsilon}^{-1} \simeq \mathbf{I} - (\mathbf{K}_{n,\varepsilon}^{-1} + \mathbf{S}_i) \text{ and } \boldsymbol{\Phi}_{0,\varepsilon}^{-1} - \boldsymbol{\Phi}_{1,\varepsilon}^{-1} \simeq \Delta\mathbf{S}. \tag{B4}$$

Using $\boldsymbol{\Sigma}_n^{-1} = \sigma_n^{-2}\mathbf{I}$ and Eq. (B4), (B3) becomes

$$\lambda(\mathbf{g}, \varepsilon) \simeq \frac{\sigma_{obj}^2}{2}\mathbf{g}^t\mathbf{H}\left(\sigma_{obj}^2\mathbf{H}\mathbf{H}^t + \varepsilon\sigma_n^2\mathbf{I}\right)^{-1}\Delta\mathbf{S} \times \left(\sigma_{obj}^2\mathbf{H}^t\mathbf{H} + \varepsilon\sigma_n^2\mathbf{I}\right)^{-1}\mathbf{H}^t\mathbf{g}, \tag{B5}$$

and, in the limit,

$$\lambda(\mathbf{g}) = \lim_{\varepsilon\to 0^+}\lambda(\mathbf{g}, \varepsilon) = \frac{1}{2\sigma_{obj}^2}\mathbf{g}^t(\mathbf{H}^+)^t\Delta\mathbf{S}\,\mathbf{H}^+\mathbf{g}, \tag{B6}$$

$$\lambda(\mathbf{g}) \simeq \frac{1}{2}\mathbf{g}_{PI}^t\Delta\mathbf{S}\,\mathbf{g}_{PI}.$$

$\mathbf{H}^+ = \lim_{\varepsilon\to 0^+}[(\mathbf{H}^t\mathbf{H} + \varepsilon\sigma_n^2\sigma_{obj}^{-2}\mathbf{I})^{-1}\mathbf{H}^t]$ is the pseudo-inverse of the system matrix[17] and $(\mathbf{H}^+)^t$ is its transpose. Also, $\mathbf{g}_{PI} = \mathbf{B}_{PI}^t\mathbf{g}$, where $\mathbf{B}_{PI}^t = \sigma_{obj}^{-1}\mathbf{H}^+$ is a scaled, reduced-rank version of the MV beamformer that accommodates ill-conditioned matrices.[35] Comparing $\mathbf{B}_{PI}^t$ with $\mathbf{B}_{MV}^t$ in Eq. (21), we see they are essentially equivalent when $\mathbf{\Sigma}_n = \sigma_n^2\mathbf{I}$, except for the regularization offered by the pseudoinverse operator. For implementation, $\mathbf{B}_{MV}^t$ also needs to be regularized to avoid ill-conditioning. These approximations to the ideal-observer strategy lead to a regularized MV beamformer, without the requirement that $\mathbf{K}_n$ is invertible.

Method 2: Alternatively, we can separate (B3) according to $\mathbf{\Phi}_{i,\varepsilon} = (\mathbf{I} + \mathbf{K}_{n,\varepsilon}^{-1}) + \mathbf{S}_i$. Following the technique shown in (23), where now $\mathbf{\Phi}_s^{-1} = \mathbf{I} + \mathbf{K}_{n,\varepsilon}^{-1}$, we use the first-order approximation

$$\mathbf{\Phi}_{i,\varepsilon}^{-1} \simeq (\mathbf{I} + \mathbf{K}_{n,\varepsilon}^{-1})^{-1} - (\mathbf{I} + \mathbf{K}_{n,\varepsilon}^{-1})^{-1}\mathbf{S}_i(\mathbf{I} + \mathbf{K}_{n,\varepsilon}^{-1})^{-1}. \tag{B7}$$

Consequently,

$$\mathbf{\Phi}_{0,\varepsilon}^{-1} - \mathbf{\Phi}_{1,\varepsilon}^{-1} \simeq (\mathbf{I} + \mathbf{K}_{n,\varepsilon}^{-1})^{-1}\Delta\mathbf{S}(\mathbf{I} + \mathbf{K}_{n,\varepsilon}^{-1})^{-1}, \tag{B8}$$

and substituting (B8) into (B3), we obtain

$$\lambda(\mathbf{g},\varepsilon) \simeq \frac{\sigma_{obj}^2}{2\sigma_n^4}\mathbf{g}^t\mathbf{H}(\mathbf{K}_{n,\varepsilon} + \mathbf{I})^{-1}\Delta\mathbf{S}(\mathbf{K}_{n,\varepsilon} + \mathbf{I})^{-1}\mathbf{H}^t\mathbf{g}. \tag{B9}$$

In the limit of $\varepsilon \to 0^+$, $\sigma_n^2(\mathbf{K}_{n,\varepsilon} + \mathbf{I}) \to \sigma_{obj}^2\mathbf{H}^t\mathbf{H} + \sigma_n^2\mathbf{I} = \mathbf{\Omega}_s$, and therefore, (B9) becomes

$$\lambda(\mathbf{g}) \simeq \frac{\sigma_{obj}^2}{2}\mathbf{g}^t\mathbf{H}\mathbf{\Omega}_s^{-1}\Delta\mathbf{S}\mathbf{\Omega}_s^{-1}\mathbf{H}^t\mathbf{g}, \tag{B10}$$

$$\lambda(\mathbf{g}) \simeq \frac{1}{2}\mathbf{g}_{WF}^t\Delta\mathbf{S}\mathbf{g}_{WF}.$$

$\mathbf{g}_{WF} = \mathbf{B}_{WF}^t\mathbf{g}$ is the beamformed RF echo signal in (26) that results from the WF beamformer $\mathbf{B}_{WF}$.

Each linear beamformer is represented in the ideal-observer analysis as a filter which is applied to the set of received echo signals in the beam, and results in the summed RF echo signals. The MV must be regularized when $\mathbf{K}_n$ is not full rank, whereas the WF beamformer is naturally regularized by the acquisition noise in the data. Specifically, $\mathbf{K}_{n,\varepsilon}^{-1}$ appears as a factor in (B5) for the MV beamformer while $(\mathbf{K}_{n,\varepsilon} + \mathbf{I})^{-1}$ appears as a factor in (B9) for the WF beamformer. Thus, we expect the WF beamformer to be more robust than the MV beamformer.

## APPENDIX C: MW BEAMFORMER

In this appendix, we derive the closed-form of the MW beamformer, which involves Wiener filtering after using the MF to compress the pre-summed echo data $\mathbf{g}_{MF}$. By multiplying both side of Eq. (2) with a MF $\mathbf{B}_{MF} = \mathbf{H}^t$, we obtain

$$\mathbf{g}_{MF} = \mathbf{H}^t\mathbf{g} = \mathbf{H}_{MF}\mathbf{f} + \mathbf{n}_{MF}, \tag{C1}$$

where $\mathbf{H}_{MF} = \mathbf{H}^t\mathbf{H}$ and $\mathbf{n}_{MF} = \mathbf{H}^t\mathbf{n}$.

The WF applied to $\mathbf{g}_{MF}$ has the form $\mathbf{W} = \sigma_{obj}\mathbf{H}_{MF}^t\,\mathbf{\Sigma}_{s,MF}^{-1}$ [see Eq. (12)], where $\mathbf{H}_{MF}^t = \mathbf{H}^t\mathbf{H}$ and $\mathbf{\Sigma}_{s,MF}$ is the stationary part of the data covariance matrix. From the definition of the stationary part given in Eq. (7) for the $\mathbf{g}_{DS}$, we form the corresponding matrix for $\mathbf{g}_{MF}$, given by

$$\mathbf{\Sigma}_{s,MF} = \sigma_{obj}^2\mathbf{H}_{MF}\mathbf{H}_{MF}^t + \sigma_n^2\mathbf{H}^t\mathbf{H} = \mathbf{H}^t\mathbf{H}(\sigma_{obj}^2\mathbf{H}^t\mathbf{H} + \sigma_n^2\mathbf{I}). \tag{C2}$$

The WF implementation requires the inversion of $\mathbf{\Sigma}_{s,MF}$. It means that $\mathbf{H}^t\mathbf{H}$ must be nonsingular. Under this assumption, the term $\mathbf{H}^t\mathbf{H}$ inside $\mathbf{\Sigma}_{s,MF}^{-1}$ can be eliminated with $\mathbf{H}_{MF}^t$ outside. Thus, the WF becomes

$$\mathbf{H}_{MF}^t\mathbf{\Sigma}_{s,MF}^{-1} = (\sigma_{obj}^2\mathbf{H}^t\mathbf{H} + \sigma_n^2\mathbf{I})^{-1}. \tag{C3}$$

The filter is applied to $\mathbf{g}_{MF} = \mathbf{H}^t\mathbf{g}$, which gives us the WF beamformer in Eq. (26). However, it requires model modifications for a nonsingular $\mathbf{H}^t\mathbf{H}$. By using the same reduced-rank approximation adopted in the MV implementation, the MW beamformer serves as a transition step between the MV and the WF.

## APPENDIX D: MATRIX-INVERSION LEMMA

Woodbury and others proposed the following identity for arbitrary matrices $\mathbf{A}$, $\mathbf{B}$, $\mathbf{C}$, and $\mathbf{D}$,[12,36]

$$(\mathbf{A} + \mathbf{BCD})^{-1} = \mathbf{A}^{-1} - \mathbf{A}^{-1}\mathbf{B}(\mathbf{C}^{-1} + \mathbf{DA}^{-1}\mathbf{B})^{-1}\mathbf{DA}^{-1}.$$

The stipulation is that $\mathbf{A}$ and $\mathbf{C}$ be nonsingular.


[1]K. E. Thomenius, "Evolution of ultrasound beamformers," in *Proceedings of the IEEE Ultrasonics Symposium* (1996), pp. 1615–1622.
[2]J. A. Mann and W. F. Walker, "A constrained adaptive beamformer for medical ultrasound: Initial results," in *Proceedings of the IEEE Ultrasonics Symposium* (2002), pp. 1807–1810.
[3]J. Li, P. Stoica, and Z. Wang, "On robust Capon beamforming and diagonal loading," IEEE Trans. Signal Processing **51**(7), 1702–1715 (2003).
[4]Z. Wang, J. Li, and R. Wu, "Time-delay- and time-reversal-based robust Capon beamformers for ultrasound imaging," IEEE Trans. Med. Imaging **24**(10), 1308–1322 (2005).
[5]M. Sasso and C. Cohen-Bacrie, "Medical ultrasound imaging using the fully adaptive beamformer," in *Proceedings of the IEEE International Conference on Acoustics, Speech, and Signal Processing* (2005), pp. 489–492.
[6]J.-F. Synnevåg, A. Austeng, and S. Holm, "Adaptive beamforming applied to medical ultrasound imaging," IEEE Trans. Ultrasonics Ferroelectrics Frequency Control **54**(8), 1606–1613 (2007).
[7]J.-F. Synnevåg, A. Austeng, and S. Holm, "Benefits of minimum-variance beamforming in medical ultrasound imaging," IEEE Trans. Ultrasonics Ferroelectrics Frequency Control **56**(9), 1868–1979 (2009).
[8]J. Capon, "High-resolution frequency-wavenumber spectrum analysis," Proc. IEEE **57**(8), 1408–1418 (1969).
[9]O. L. Frost III, "An algorithm for linearly constrained adaptive array processing," Proc. IEEE **60**(8), 926–935 (1972).
[10]C.-I. C. Nilsen and S. Holm, "Wiener beamforming and the coherence factor in ultrasound imaging," IEEE Trans. Ultrasonics Ferroelectrics Frequency Control **57**(6), 1329–1346 (2010).
[11]Y.-H. Wang and P.-C. Li, "SNR-dependent coherence-based adaptive imaging for high-frame-rate ultrasonic and photoacoustic imaging," IEEE

Trans. Ultrasonics Ferroelectrics Frequency Control **61**(8), 1419–1432 (2014).
[12]H. L. Van Trees, *Detection, Estimation, and Modulation Theory, Part IV, Optimum Array Processing* (Wiley, New York, 2002).
[13]S. Gannot and I. Cohen, "Adaptive beamforming and postfiltering," in *Springer Handbook of Speech* Processing, edited by J. Benesty, M. M. Sonhi, and Y. A. Huang (Springer-Verlag, Berlin, Germany, 2008), pp. 945–978.
[14]K-.S. Kim, J. Liu, and M. F. Insana, "Efficient array beam forming by spatial filtering for ultrasound B-mode imaging," J. Acoust. Soc. Am. **120**(2), 852–861 (2006).
[15]T. L. Szabo, *Diagnostic Ultrasound Imaging: Inside Out*, 2nd ed. (Elsevier Science, Boston, MA, 2014).
[16]International Commission on Radiation Units and Measurements, *Medical Imaging: The Assessment of Image Quality* (Bethesda, MD, 1996).
[17]H. H. Barrett and K. J. Myers, *Foundations of Image Science* (John Wiley and Sons, Hoboken, NJ, 2004).
[18]C. K. Abbey, R. J. Zemp, J. Liu, K. K. Lindfors, and M. F. Insana, "Observer efficiency in discrimination tasks simulating malignant and benign breast lesions with ultrasound," IEEE Trans. Med. Imaging **25**(2), 198–209 (2006).
[19]N. Q. Nguyen, C. K. Abbey, and M. F. Insana, "An adaptive filter to approximate the Bayesian strategy for sonographic beamforming," IEEE Trans. Med. Imaging **30**(1), 28–37 (2011).
[20]C. K. Abbey, N. Q. Nguyen, and M. F. Insana, "Optimal beamforming in ultrasound using the ideal observer," IEEE Trans. Ultrasonics Ferroelectrics Frequency Control **57**(8), 1782–1796 (2010).
[21]J. A. Jensen and N. B. Svendsen, "Calculation of pressure fields from arbitrarily shaped, apodized, and excited ultrasound transducers," IEEE Trans. Ultrasonics Ferroelectrics Frequency Control **39**(2), 262–267 (1992).
[22]J. A. Jensen, "Field: A program for simulating ultrasound systems," Med. Biol. Eng. Comput. **34**, 351–353 (1996).
[23]P. Tortoli, L. Bassi, A. Dallai, F. Guidi, and S. Ricci, "ULA-OP: An advanced open platform for ultrasound research," IEEE Trans. Ultrasonics Ferroelectrics Frequency Control **56**(10), 2207–2216 (2009).
[24]N. Q. Nguyen, C. K. Abbey, and M. F. Insana, "Objective assessment of sonographic quality I: Task information," IEEE Trans. Med. Imaging **32**(4), 683–690 (2013).
[25]N. Q. Nguyen, C. K. Abbey, and M. F. Insana, "Objective assessment of sonographic quality II: Acquisition information spectrum," IEEE Trans. Med. Imaging **32**(4), 691–698 (2013).
[26]R. J. Zemp, C. K. Abbey, and M. F. Insana, "Linear system models for ultrasonic imaging: Application to signal statistics," IEEE Trans. Ultrasonics Ferroelectrics Frequency Control **50**(6), 642–654 (2003).
[27]M. F. Insana and D. G. Brown, "Acoustic scattering theory applied to soft biological tissues," in *Ultrasonic Scattering in Biological Tissues*, edited by K. K. Shung and G. A. Thiemes (CRC Press, Boca Raton, FL, 1993).
[28]J. Ng, R. Prager, N. Kingsbury, G. Treece, and A. Gee, "Wavelet restoration of medical pulse-echo ultrasound images in an EM framework," IEEE Trans. Ultrasonics Ferroelectrics Frequency Control **54**(8), 550–568 (2007).
[29]American College of Radiology, *Breast Imaging Report and Data System Atlas* (Reston, VA, 2003).
[30]H. L. Van Trees, *Detection, Estimation, and Modulation Theory, Part I*. (John Wiley and Sons, New York, 1968).
[31]G. H. Golub and C. F. Van Loan, *Matrix Computations*, 3rd ed. (The Johns Hopkins University Press, Baltimore, MD, 1996).
[32]J. Krolik, "The performance of matched-field beamformers with Mediterranean vertical array data," IEEE Trans. Signal Processing **44**(4), 2605–2611 (1996).
[33]R. F. Wagner, S. W. Smith, J. M. Sandrik, and H. Lopez, "Statistics of speckle in ultrasound B-scans," IEEE Trans. Sonics Ultrasonics **30**(3), 156–163 (1983).
[34]S. W. Smith, R. F. Wagner, J. M. Sandrik, and H. Lopez, "Low contrast detectability and contrast/detail analysis in medical ultrasound," IEEE Trans. Sonics Ultrasonics **30**(3), 164–173 (1983).
[35]R. G. Lorenz and S. P. Boyd, "Robust minimum variance beamforming," IEEE Trans. Signal Processing **53**(5), 1684–1696 (2005).
[36]M. A. Woodbury, *Inverting Modifies Matrices*. Memorandum Rep. 42, Statistical Research Group, Princeton, NJ (1950).